Journal of Physics and Chemistry of Solids 162 (2022) 110526

Contents lists available at ScienceDirect

Journal of Physics and Chemistry of Solids

journal homepage: www.elsevier.com/locate/jpcs

Alkali-metal induced electronic structure evolution in Sn_4Sb_3 studied by angle-resolved photoemission spectroscopy

Wei Wen [a,b], Xu Duan [a,b], Bin Liu [a,b], Caiyun Hong [a,b], Zhen Song [a,b], Bing Lin [a,b], Pengxu Ran [a,c], Shi Liu [b], Zhi Ren [b], Rui-Hua He [b,*]

[a] Department of Physics, Fudan University, Shanghai, 200433, China
[b] Key Laboratory for Quantum Materials of Zhejiang Province, School of Science, Westlake University, Hangzhou, 310024, Zhejiang, China
[c] Department of Physics, Zhejiang University, Hangzhou, 310027, Zhejiang, China

ARTICLE INFO

Keywords:
Angle-resolved photoemission spectroscopy
Topological semimetal
Alkali metal dosing
Intercalation
Dirac cone

ABSTRACT

We report on an angle-resolved photoemission spectroscopy study of the effect of *in-situ* cesium (Cs) dosing on the surface electronic structure of Sn_4Sb_3, a newly emerging candidate of topological semimetallic superconductor. As the chemical potential of the system increases upon Cs dosing, we observed an electronic structure evolution that features an increasing sharpness of band features as well as a momentum- and band-dependent energy shift of the bands at low binding energies. These observations go beyond a simple rigid band shift model and are manifestations of quantum confinement of electronic states near the surface due to Cs decoration. By studying the evolution of Cs 5*p* core level as functions of Cs dosage and photoelectron emission angle, we found Cs atoms deposit on the sample surface at low dosages and tend to intercalate underneath the surface at high dosages. This process is accompanied by a gradual suppression of a surface band splitting, an observation that can be captured by simplified first-principles calculations in both cases with the deposition/intercalation occurring on top of/underneath the first Sn–Sb bilayer. Our finding highlights an intriguing possibility of an unexpected dimensionality reduction in Sn_4Sb_3 caused by Cs intercalation at interstitial sites that promises its novel surface properties different from the bulk.

1. Introduction

Nowadays, *in-situ* alkali metal surface dosing has become a prevalent approach in quantum materials research based on angle-resolved photoemission spectroscopy (ARPES). Deposited alkali metal atoms tend to lose electrons to the materials surface underneath, causing an effective electron doping of the topmost atomic layers that are directly probed by the surface-sensitive ARPES. Electron doping results in increases in both the electron chemical potential of most materials (with few exceptions [1]) and in the population of unoccupied states otherwise inaccessible to ARPES [2,3]. This is a versatile doping method that has been applied to a variety of materials showing a doping capacity largely dependent on the nature of substrate material and dosing species. It allows information about continuous doping evolution to be obtained on the same sample surface without complications arising from the traditional use of multiple samples at different bulk doping levels [4,5].

Alkali metal surface dosing also brings about new physics. Alkali metal cations together with the transferred electrons set up an electrostatic potential with a strong variation in the near surface region that causes surface band bending as well as an effective spatial confinement and, in many cases, emergence of quantum-well-like states [6–9]. Such quantum confinement is believed to be the underlying cause for the numerous novel phenomena arising from alkali metal surface dosing, such as surface Stark effect [6,10–13], dimensionality reduction [7,8,14–17], and topological Lifshifz transition [18]. A unified picture for the quantum confinement will guide new discoveries, further understanding and exploitations of new physics.

This, unfortunately, has not yet been available due to the following complications. While in most studies dosed species were found or presumed to adsorb on the sample surfaces, they can migrate into the van der Waals (vdW) gap in layered materials, leading to the so-called intercalation that is prone to occur at room temperature [19] and was also found in studies even with the samples held at low temperatures [14,16,20]. In the case of alkali metal surface adsorption, the effect of quantum confinement on the surface electronic structure can be

* Corresponding author.
E-mail address: heruihua@westlake.edu.cn (R.-H. He).

https://doi.org/10.1016/j.jpcs.2021.110526
Received 24 November 2021; Accepted 2 December 2021
Available online 4 December 2021

modelled quite well for dosed semiconductors that only involve accumulation of electron-like states from the conduction bands. Whereas in semimetals, the situation becomes more complex due to the existence of both hole-like and electron-like free carriers that tend to accumulate in different spatial regions below the surface [15]. As for the case of alkali metal intercalation, its effect on the surface electronic structure largely depends on the depth of intercalation sites and, in layered semimetals with a relatively large c-axis lattice constant, is expected to be small due to a large distance of the topmost vdW gap from the surface and a sizable electrostatic screening.

In this paper, we present a possible rare example of *in-situ* alkali metal intercalation at interstitial sites near the surface of a vdW layered semimetal, which contributes a significant new piece to shaping a unified picture for the quantum confinement. We have performed an ARPES study of the effect of *in-situ* Cs dosing on the surface electronic structure of Sn_4Sb_3, a topological semimetal with a large c-axis lattice constant. We observed clear manifestations of quantum confinement of electronic states near the surface due to Cs decoration. Dosage and angle dependences of the Cs core-level spectroscopy reveal distinct channels for Cs dosing, with signatures of intercalation that dominates at high dosages. Such intercalation likely occurs at the interstitial sites within the structural block with covalent bonding, and causes a partial electronic decoupling between the topmost Sn and Sb layers on top of their structural decoupling from the bulk. This might result in a suppression of a surface band splitting as observed in experiment and captured by first-principles calculations. This finding highlights the possibility of a unique dimensionality reduction in Sn_4Sb_3 that promises its novel surface properties different from the bulk.

2. Material and methods

High-quality single crystals of Sn_4Sb_3 were grown by a flux growth method [21,22]. ARPES experiments were performed in the home laboratory at Westlake University using He–I light (21.2 eV; unless specified otherwise), and a Scienta DA30-L spectrometer with a total energy resolution of 12 meV. Samples were cleaved in a vacuum better than 1×10^{-10} mbar at the measurement temperature around 6 K. High-purity Cs atoms were dosed *in-situ* from a commercial alkali-metal source (by Fermi Instruments) onto the surface of sample maintained at the measurement temperature. The alkali-metal source was well degassed (for several weeks) prior to evaporation with a maximal increment in pressure below 3×10^{-11} mbar. A steady dosing rate can be achieved during the entire experiment, which is controlled by the electric current heating the Cs-containing cartridge and calibrated using a quartz crystal thickness monitor. Compared with the case with typical alkali-metal getter sources, this allows a more precise control of Cs dosage that is proportional to the cumulative time of evaporation at a fixed current value. Low-energy electron diffraction (LEED) pattern was recorded after sample cleaving that indicates absence of surface reconstruction (Fig. 1 (e)). Earlier ARPES experiments (results not shown) were also performed at the BL5U beamline of the UVSOR-II Synchrotron Facility, Institute for Molecular Science, Japan using a MBS A-1 spectrometer, and at the BL03U beamline of the Shanghai Synchrotron Radiation Facility using a Scienta DA30-L spectrometer.

First-principles calculations for simplified slab models are carried out using plane-wave basis density functional theory (DFT) as implemented in the Vienna Ab-initio Simulation Package (VASP) [23,24]. To ensure convergence, we employed an energy cut-off of 400 eV and $8 \times 8 \times 1$ Γ-centered *k*-mesh to converge the total energy to 1 meV per cell. The Perdew, Burke, and Ernzerhof parameterization (PBE) of generalized gradient approximation (GGA) [25] to the exchange correlation functional was employed, with which the atomic positions are fully optimized until the residual force on each atom is less than 0.001 eV/Å. To model atomic slabs, we built more than 15 Å vacuum along the out-of-plane direction and incorporated spin-orbit coupling in the calculations. Results of the full-fledged first-principles bulk and slab calculations are reproduced from our earlier study [26].

3. Results

3.1. Structural properties

The unit cell of Sn_4Sb_3 consists of three equivalent septuple-layer blocks, each comprising seven alternating atomic layers in the sequence of Sn–Sb–Sn–Sb–Sn–Sb–Sn that are covalently bonded (Fig. 1 (a)). The three septuple-layer blocks are stacked along the c-axis with a

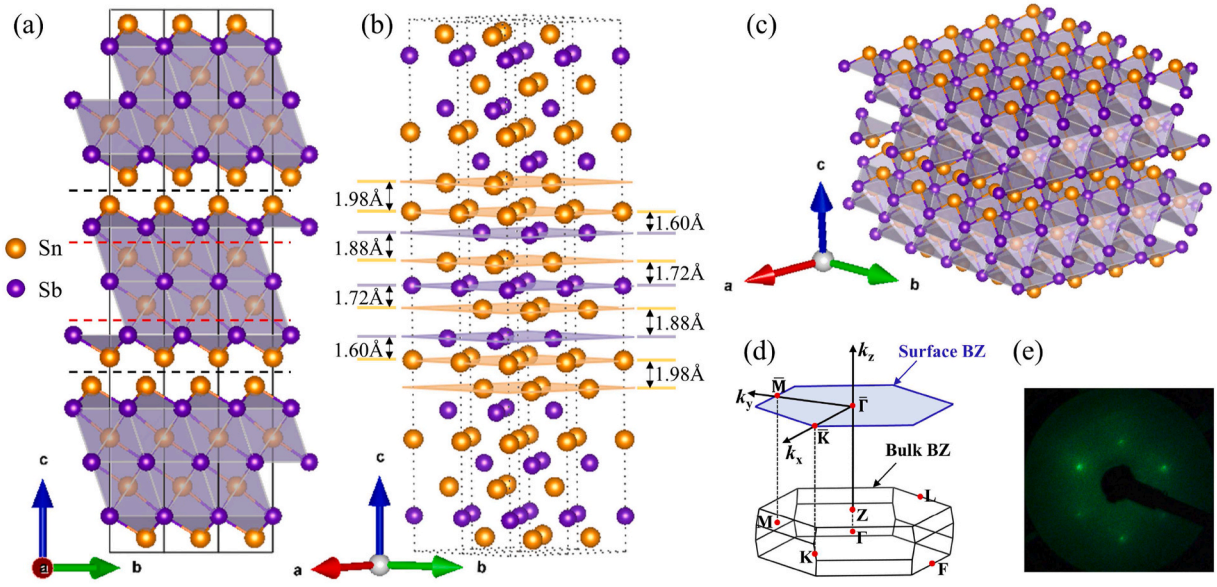

Fig. 1. Schematic drawing of the (a) side view, (b) and (c) perspective view of the crystal structure of Sn_4Sb_3. Black and red dashed lines in (a) indicate natural cleavage planes for Cs adsorption and the interstitial sites for Cs intercalation, respectively. Characteristic spacings between different atomic layers within a c-axis unit cell are marked in (b). In (c), a Sn monolayer of hexagonal symmetry is exposed on the surface after cleaving. (d) Schematic drawing of the 3D (black) and projected 2D (blue) Brillouin zone (BZ) of rhombohedral primitive cell with high-symmetry points as marked. (e) LEED pattern obtained on a freshly cleaved Sn_4Sb_3 sample with 100 eV beam energy. (For interpretation of the references to colour in this figure legend, the reader is referred to the Web version of this article.)

periodicity of 37.3 Å, and interact weakly through vdW interaction across a vdW gap of 1.98 Å (Fig. 1(b)). The black dashed lines in Fig. 1(a) indicate the natural cleavage planes between neighboring septuple-layer blocks, resulting in a pure surface termination with a Sn layer of hexagonal planar symmetry after cleaving (Fig. 1(c)). This surface Sn layer is far from free-standing due to its covalent bonding with the underlying Sb layer of the same symmetry. The Sn–Sb interlayer spacing is 1.60 Å, the smallest among all other spacings in Sn_4Sb_3 (Fig. 1(b)). This tightly-binded Sn–Sb bilayer sits on top of another Sn–Sb bilayer, with the largest interlayer spacing (1.88 Å) within the septuple-layer block and only second to the vdW gap within the unit cell.

3.2. Electronic structure

3.2.1. Pristine sample

To set a stage for the comparison with the case after Cs dosing, we first recap several important features near the Fermi level (E_F) in the electronic structure of pristine Sn_4Sb_3 that we recently found [26]. Our full-fledged slab calculations therein highlight three sets of surface-related states (as red coded in Fig. 2(e) and (f) and) that can be identified in experiment (cf. Fig. 2(a) and (b)): a pair of band-splitting-like features, SS1′ and SS1″, centered at $\overline{\Gamma}$ and about energy E-E_F = -0.4 eV with a separation ~0.134 eV; a hole-like band, SS2, crossing E_F along $\overline{\Gamma}$-$\overline{K}$ ($\overline{\Gamma}$ –$\overline{K'}$); another hole-like band, SS3, centered at $\overline{\Gamma}$ and at E-E_F < -0.7 eV. Specifically, SS1′ and SS1″ have been ascribed to be the antibonding and bonding bands due to the hybridization between the surface Sn 5*p* orbitals and the subsurface Sb 5*p* orbitals (hence the symbol "SS" for surface states), based on a systematic study of their evolution upon changing X in the Sn_4X_3 (X = P, As, Sb) family [26]. Other bands as black coded in Fig. 2(e) and (f) from states below the topmost surface layers and are associated with a substantial bulk character. Some of these slab bands find a reasonable correspondence with the bands given by the full-fledged bulk calculations, such as BS1′, BS1″, BS2, and BS3 as marked in Fig. 2(c) and (d) (cf. Fig. 2(e) and (f); "BS" for bulk bands). These bands can also be observed in experiment (Fig. 2(a) and (b)). Specifically, the electron-like band BS1′ in the calculation (Fig. 2(c) and (d)) shows up in experiment as a blob of diffused intensity that touches E_F around $\overline{\Gamma}$ (Fig. 2(a) and (b)). This is a combined result of a strong c-axis (k_z) dispersion of BS1' and the poor k_z resolution of the ARPES experiment using He–I that effectively measures an extended range in k_z around the value designated for the full-fledged bulk calculations.

3.2.2. Cs dosing evolution at low binding energies

After *in-situ* Cs dosing of a substantial amount, pronounced variations in the low-binding-energy electronic structure are observed (cf. Fig. 2(g) vs. 2(a), 2(h) vs. 2(b)). At first glance, there seems to be a rigid shift of the overall band structure, where the aforementioned three sets of surface-related states sink further below E_F. However, the band structure itself is, in fact, not "rigid". Some of the bulk bands (BS1′, BS1″ and BS2) appear sharper than in the pristine case. In particular, BS1' evolves into a distinct upward-dispersing electron-like band (cf. Fig. 2(j) vs 2(i)) that tends to connect with a downward-dispersing hole-like band evolving from BS1″, conjuring to form a Dirac cone centered at $\overline{\Gamma}$ with a Dirac point located at E-E_F ~ -0.7 eV (Fig. 2(g) and (h)). Besides, the constant-energy intensity contours at different energies measured in the same experiment from the same sample surface look much cleaner after dosing than those obtained prior to dosing (Fig. 2(k) vs. 2(l)). The increased sharpness of band features and cleanliness of intensity contours confirm that the cleaved sample surface is of a high quality and the Cs coverage is quite homogeneous on the scale of the light beam spot size (~1.2 mm).

A detailed analysis of the Cs dosing evolution of the electronic structure reveals other salient departures from the rigid band shift model. The band splitting between SS1′ and SS1″ is strongly suppressed with increasing Cs dosage, as can be seen along different in-plane directions (Fig. 3(a)-3(g) for $\overline{K'}$-$\overline{\Gamma}$-$\overline{K}$ and 3(k)-3(o) for $\overline{M'}$-$\overline{\Gamma}$-$\overline{M}$). Both bands become indistinguishable around 7-min dosage (see Fig. 3(h) and (p) for momentum positions k_1 and k_4 marked in Fig. 3(a) and (k)) and gradually develop an upward curvature (marked by the red circle in Fig. 3(f)) upon dispersing away from $\overline{\Gamma}$ toward $\overline{K}$. Not only does the overall shape of the band structure vary with Cs dosing, but also the energy separations between bands are changing because of their different energy shifts. SS1′ and SS1″ exhibit an overall downward shift in energy by ~0.2 eV, and up to 0.25 eV depending on momentum (see Fig. 3(h)-3(j) & 3(p) for momentum positions k_1-k_4 marked in Fig. 3(a) and (k)). While surface-related states, such as SS2 and SS3, undergo similar downward shifts of ~0.18 eV (Fig. 3(i) and (j)) the bulk states as well as the 2D states emerging from the bulk states upon Cs dosing have qualitatively different behaviors. While BS3 shifts by ~0.11 eV at $\overline{\Gamma}$ (Fig. 3(i)), the Dirac cone derived from BS1' and BS1", once fully developed, shows an overall downward shift of less than 0.1 eV (as guided by the red arrows in Fig. 3(e)-3(g) & 3(m)-3(o)). In contrast, virtually no energy shift is observed on BS2, as indicated by the lack of momentum shift at a given energy position (see Fig. 3(q) for energy position E_1 marked in Fig. 3(k)). The observed momentum- and band-dependent energy shift further supports the non-rigid band nature of the electronic structure evolution upon Cs dosing in Sn_4Sb_3.

3.2.3. Cs dosing evolution at core levels

Our Cs 5*p* core level measurement suggests the presence of distinct channels for Cs dosing. With an increasing Cs dosage from zero, the Cs $5p_{1/2}$ and $5p_{3/2}$ multiplets first emerge and grow in intensity while maintaining their peak positions (Fig. 4(a)). A shoulder feature develops on the low-binding-energy slope of each multiple peak upon approaching the amount of 10-min dosage. It becomes dominant at 16 min, producing a symmetric peak at the original shoulder position. In contrast, the multiplet peaks at low dosages display clear asymmetric line shapes with prolonged tails extending toward low binding energy, which signals the presence of a hidden second spectral component. More quantitative information can be extracted based on a global fit to the core level spectra measured at different dosages by assuming for each multiplet two peaks with fixed (dosage independent) energy positions and peak widths. As similar spectral behaviors are seen for both multiplets, we perform such an analysis only on the $5p_{3/2}$ multiplet, with the fitting results shown in Fig. 4(b). While the intensity of the blue peak (Cs_2) corresponding to the shoulder feature increases monotonically, that of the green peak (Cs_1) shows a non-monotonic behavior that almost vanishes at 16 min, as summarized in Fig. 4(c). The presence of two peaks for the Cs multiplet is an indication of two different types of sites in different chemical environments for hosting the dosed Cs atoms. The dosage dependence of the peak intensity suggests that Cs dosing mainly takes place at one type of sites (corresponding to Cs_1) at low dosages while the other type (corresponding to Cs_2) dominates at high dosages.

Photoelectron emission angle dependence of the Cs 5*p* core level spectrum sheds light on the nature of the latter type of dosing sites at high dosages (Fig. 4(d)). At about 16-min dosage, where the low-binding-energy (blue) peak already dominates in the core level spectrum (Fig. 4(c)), we observe a monotonic decrease in the photoemission intensity with increasing photoelectron emission angle (θ, defined w.r.t. the sample normal), as shown in Fig. 4(d) for the results of curve fitting with a single peak for Cs_2 (with the small Cs_1 contribution ignored). We note that disordered chemical species adsorbed on a surface are expected to yield a weak, if not null, angle dependence for the photoemission intensity variation of the core levels due to the orientational disorder of related atomic orbitals. In contrast, photoelectrons emitted from species below a surface are obstructed from the atoms in the surface overlayer, giving rise to an approximate $\exp(-d/\lambda/\cos\theta)$ (where d is the thickness of the overlayer, λ the inelastic mean free path of

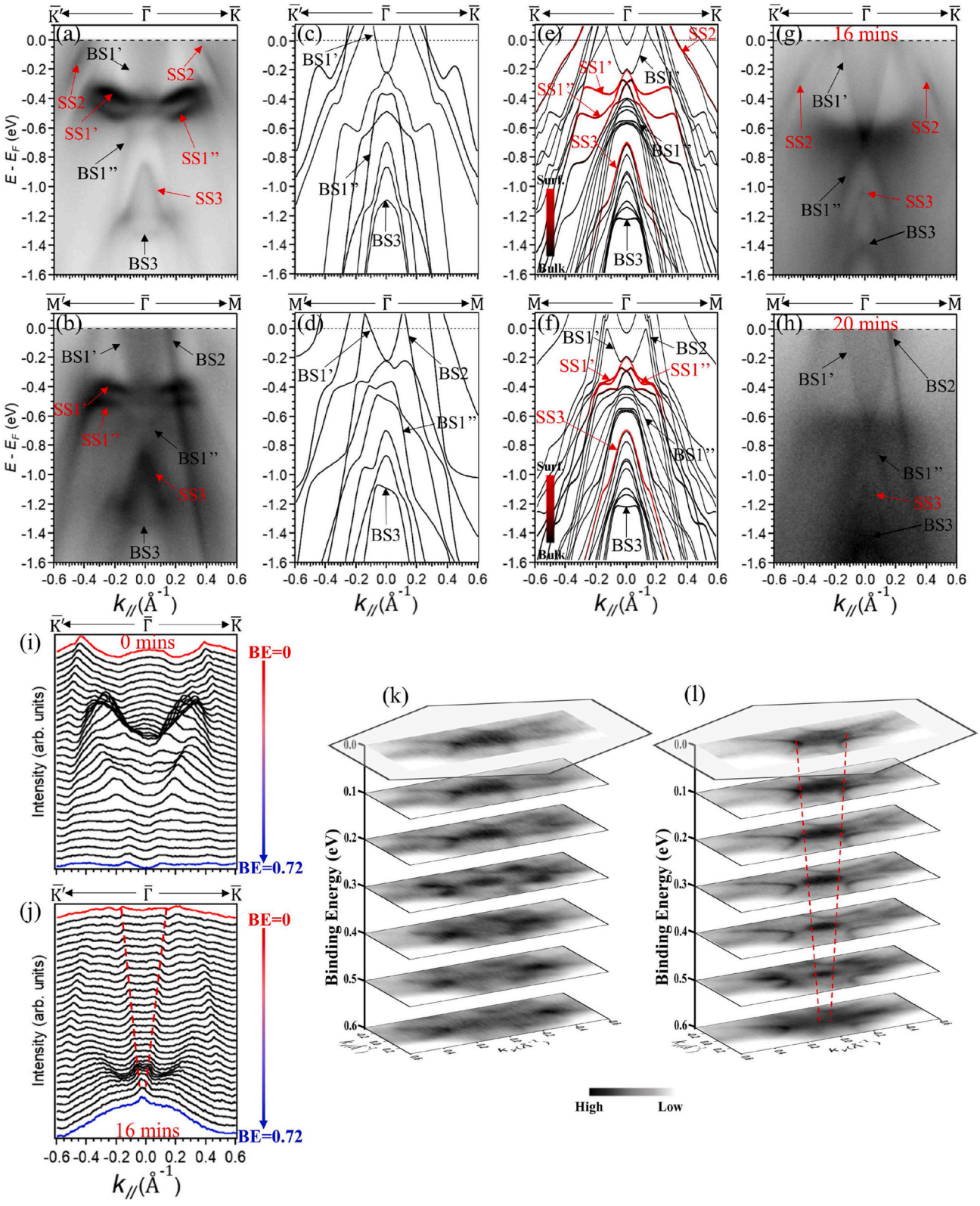

Fig. 2. Electronic structure of pristine Sn_4Sb_3: (a) and (b) Band dispersion images measured along $\overline{K}'$-$\overline{\Gamma}$-$\overline{K}$ and $\overline{M}'$-$\overline{\Gamma}$-$\overline{M}$ directions, respectively; (i) momentum distribution curves (MDCs; energy integration window ±7 meV; vertically offset for clarity) for (a) within the binding energy (BE) range as labelled; (k) constant-energy intensity contours within the first Brillouin zone (hexagon) stacked along the binding energy axis (energy integration window ±15 meV). (g), (h), (j) and (l) Corresponding results after Cs dosing of a substantial amount (with the cumulative time of Cs evaporation as labelled). (c)–(d) and (e)–(f) Calculated band dispersions along both directions from full-fledged first-principles bulk and slab calculations (reproduced from Ref. [26]). Color scale in (e) & (f) shows the relative proportion of surface character in the calculated energy bands. Various bulk (BS1′, BS1″, BS2, BS3) and surface-related (SS1′, SS1″, SS2, SS3) states discussed in the main text are labelled. Red dashed lines in (j) and (l) are guides to the eye for the upper Dirac cone derived from BS1′ after Cs dosing. (For interpretation of the references to colour in this figure legend, the reader is referred to the Web version of this article.)

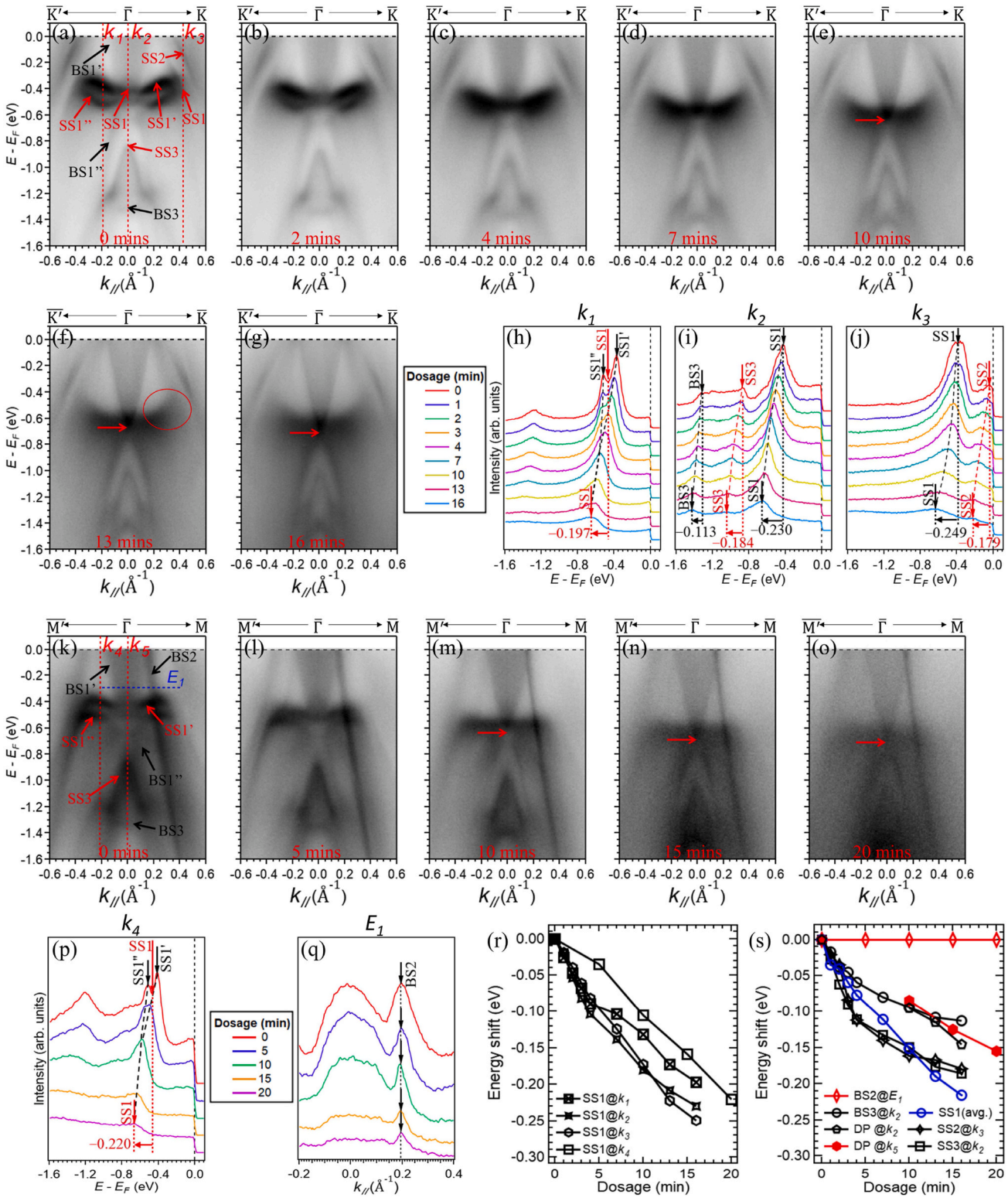

Fig. 3. Band dispersion images measured along (a)–(g) $\overline{K}$-$\overline{\Gamma}$-$\overline{K}$ and (k)–(o) $\overline{M}$-$\overline{\Gamma}$-$\overline{M}$ directions at different Cs dosages (with the cumulative time of Cs evaporation as labelled). Red arrow points out the position of the Dirac point of the Dirac cone that becomes well-defined with dosing. (h)–(j) and (p) Dosage-dependent energy distribution curves (EDCs; vertically offset for clarity) at the momentum positions k_1~k_3 and k_4 as marked respectively in (a) and (k), along with related band features and their relative shifts in energy with dosing as marked. (q) MDCs (vertically offset for clarity) at the energy position E_1 as marked in (k). Cs dosage dependence of the relative shifts in energy (with respect to the pristine case) of various band features at different momentum positions on (r) SS1′ and SS1′′ (denoted together as SS1) and on (s) other bulk or surface-related bands (including SS1′ and SS′′ for which the averages of all the shifts in (r) are shown in blue, as well as the positions of the Dirac point (DP) as tracked along both momentum directions). Error bars reflect uncertainty in determining the feature positions and are smaller than the symbol size. (For interpretation of the references to colour in this figure legend, the reader is referred to the Web version of this article.)

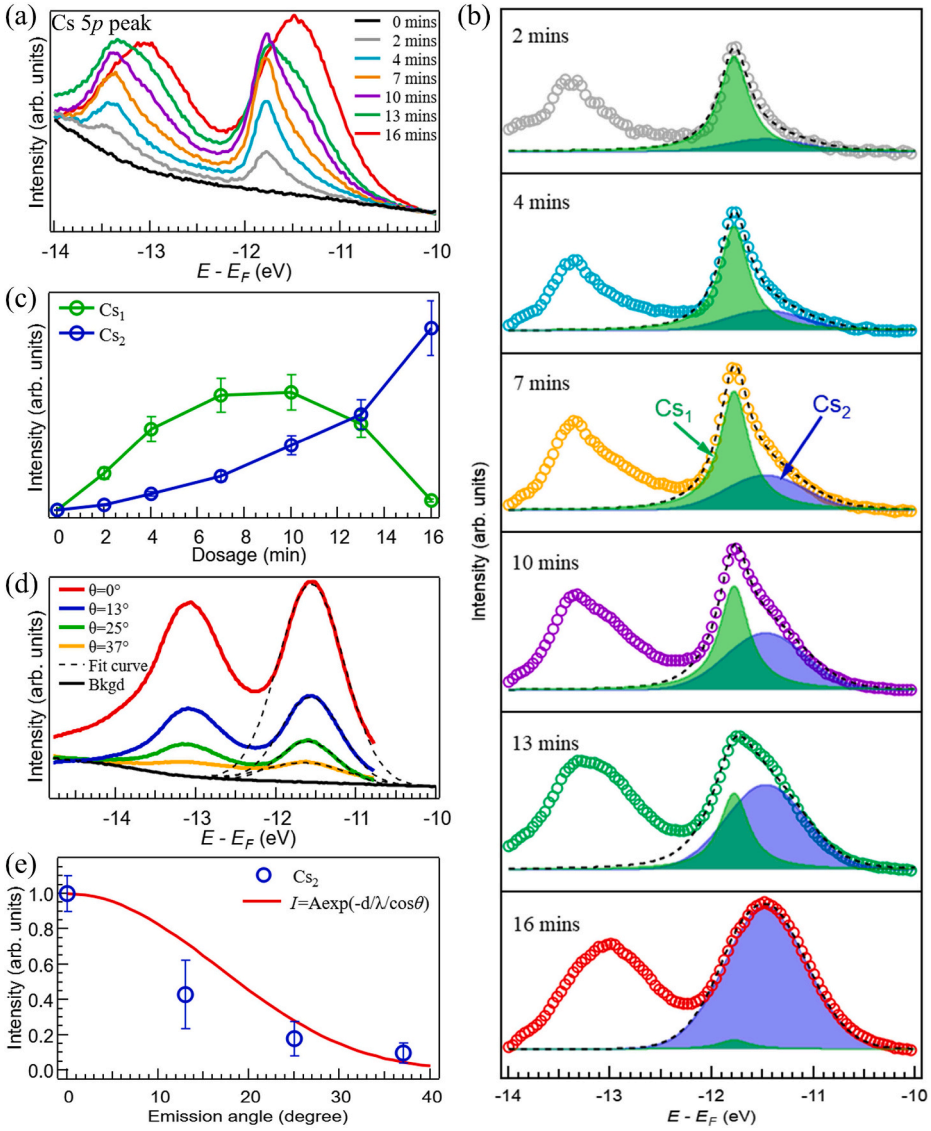

Fig. 4. (a) Cs 5*p* core-level spectra at different Cs dosages as labelled. Results of (b) the fitting curves and (c) fitted peak intensity of a global fit to the core level spectra in (a), with two Lorentzian peaks (marked as Cs_1 and Cs_2, respectively, in green and blue) of fixed (dosage independent) energy positions and peak widths (and zero background) assumed for the multiplet spectral feature located at energy around −11.8 eV. (d) Cs 5*p* core level spectra at different photoelectron emission angles (0° for normal emission) for about 16-min dosage. Dashed curve is the result of a curve fitting with a single peak, whose intensity is summarized and compared with the function $I = A\exp(-d/\lambda/\cos\theta)$ (red curve; $d/\lambda = 12$) in (e). Error bars in (c) and (e) reflect uncertainties in the curve fittings on the fitted peak intensity. All core-level spectra have been subtracted off the same 0-min spectrum in (a) [reproduced in black in (d)] obtained from the pristine sample prior to being subjected to the curve fittings in (b) and (d). Spectral intensity of all curves in (a) and (d) are normalized at −10 eV. (For interpretation of the references to colour in this figure legend, the reader is referred to the Web version of this article.)

photoelectrons) scaling of the photoemission intensity as a function of the emission angle [27,28]. Such an angle-dependent behavior was found on the core levels of alkali metals in earlier dosing studies of some layered materials, and has been taken as evidence for the alkali metal intercalation [29,30]. Therefore, a similar angle dependence of the Cs core level intensity we observe (Fig. 4(e)) supports the idea that intercalation occurs upon dosing and dominates at high Cs dosages.

3.2.4. *DFT calculations*

To elucidate the observed impacts of Cs dosing on the surface electronic structure in Sn_4Sb_3, we have performed separate DFT calculations for different slab models that involve a Sn–Sb bilayer located in different Cs environments, as depicted by the cartoons in Fig. 5. For an undosed Sn–Sb bilayer (Fig. 5(a)), such a simplified model is able to capture major features of the electronic structure observed in experiment as well as the one given by the full-fledged DFT calculation for the pristine surface (Fig. 2), such as an electron-like band that mimics BS1′, a band splitting that mimics the one between SS1′ and SS1″, and hole-like bands that mimic BS1” and SS3 (all centered at $\bar{\Gamma}$ from low to high binding energy).

With Cs atoms added to either the top or bottom of the bilayer (Fig. 5 (b) and (c)), the chemical potential of the system increases as a result of electron doping by Cs, and the dispersion associated with the band splitting develops an upward curvature upon dispersing away from $\bar{\Gamma}$, as opposed to the undosed case (Fig. 5(a)). Both aspects are also reminiscent of the experimental observations. In contrast, adding Cs in between the Sn and Sb layers leads to an almost complete decoupling of the two. The resulting band structure resembles the superposition of those of two free-standing Sn and Sb monolayers (Fig. 5(d)-5(f)) [31], and appears entirely different from the experiment. On the other hand, between the two cases with Cs placed on top and at the bottom of the Sn–Sb bilayer, there is a notable difference: the band splitting is reduced by ~30% with Cs placed on top of the bilayer (Fig. 5(b)), whereas it is substantially reduced (by ~80%) and becomes close to vanishing over a substantial momentum range around $\bar{\Gamma}$ with Cs placed at the bottom of the bilayer (Fig. 5(c)).

4. Discussion

Our observation of an increasing sharpness of low-binding-energy band features and cleanliness of constant-energy intensity contours upon Cs dosing is somewhat counterintuitive, since doping generally brings about increased disorder, thereby leading to broader, not sharper, linewidths and more blurred, not cleaner, contours [6,32]. Nevertheless, we note that, for the pristine surface, the aforementioned k_z-broadening effect is a dominant source of linewidth broadening for the bulk bands.

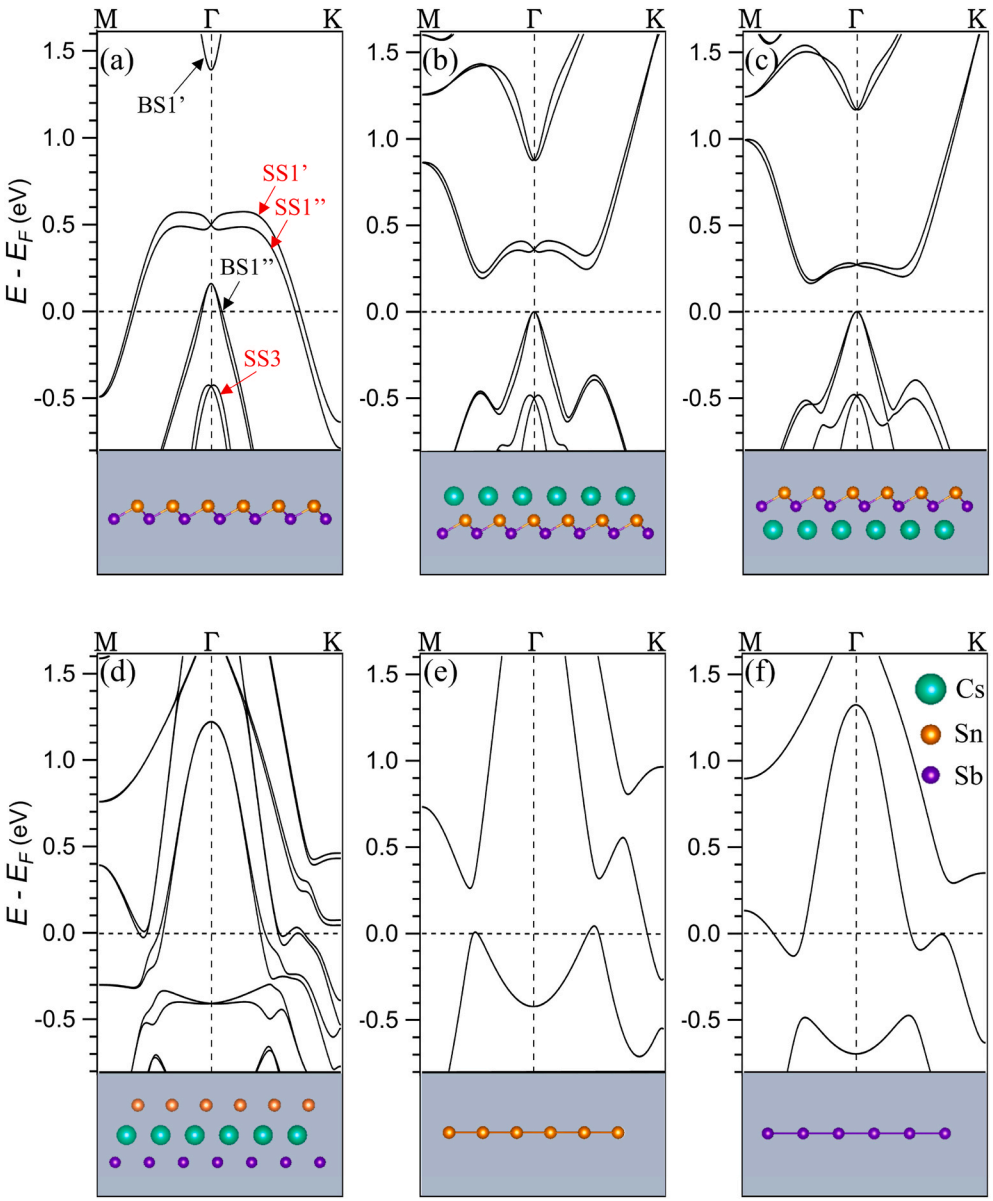

Fig. 5. (a)–(d) Band dispersions along high-symmetry directions given by DFT calculations for different slab models that involve a Sn–Sb bilayer located in different Cs environments as depicted in the cartoons. (a) for a pristine bilayer without Cs, (b) for Cs on top of the bilayer, (c) for Cs below the bilayer; (d) for Cs in the middle of the bilayer. (e)–(f) for Sn and Sb monolayers, respectively. In-plane structural parameters are fixed to the experimental value of Sn_4Sb_3 (hexagonal lattice constant 4.332 Å) for all Sn, Sb and Cs monolayers. Their inter-layer spacings and relative in-plane translations are subjected to optimization in the calculations.

The increased sharpness is therefore an experimental signature that the states that emerge after dosing have a 2D character, with wave functions confined to the topmost few layers of Sn_4Sb_3, thus suppressing the k_z broadening. Similar phenomenology has been observed in other layered materials with 3D characteristics in their bulk electronic structures [15, 32].

The observed momentum- and band-dependent energy shift of the low-binding-energy electronic structure is a clear manifestation of quantum confinement due to Cs decoration in this system. The presence of a large band-bending potential gradient near the surface results in an effective spatial confinement of electronic states, to a varied degree that depends on the spatial extension of their wave functions. Without an elaborate first-principles-based surface space charge calculation [15], we cannot specifically predict in our case how exactly a given electron band is expected to transform in the energy-momentum space with surface dosing, however, it would be reasonable to expect the following to be true. Generally speaking, states of a predominant surface nature with their wave functions being localized mostly in the region near the topmost surface are most affected, whose energies largely follow the downward variation of the potential with dosing, which is consistent with the similar trends we observed on SS1, SS2 and SS3 (Fig. 3(r) and (s)). Whereas, states of a considerable bulk character with their wave functions being extended substantially beyond the tail region of the band-bending potential are less affected, exhibiting smaller overall shifts in energy, as we observed on BS3 and the Dirac cone states derived from BS1' and BS1'', or even negligible shifts, as on BS2 (Fig. 3(s)).

Dosing evolution of the Cs core levels reveals two distinct channels for Cs dosing in our system. Alkali metal dosing in layered materials can in principle occur in three ways, i.e., adsorption on the sample surface, intercalation into the vdW gaps between the neighboring structural blocks with covalent bonding, and intercalation into the interstitial sites within these structural blocks. While the intercalation into the vdW gaps can occur in Sn_4Sb_3 which has a large c-axis lattice constant (37.3 Å), it is expected to have a small effect on the surface electronic structure because the intercalation sites are located (at about 12.4 Å) far away from the surface beyond the electrostatic screening length. These vdW intercalated Cs atoms are not supposed to be detected in our core level experiment using He–I light, owing to the short inelastic mean free path (of a few Å) of the emitted photoelectrons. Therefore, Cs intercalation into the vdW gaps is likely irrelevant to our observation.

On the other hand, the emission angle dependence study of the Cs core levels clearly points to the relevance of intercalation at high Cs dosages. Hence, this can only occur at the interstitial sites within the topmost septuple-layer block. In order to be detectible in core-level experiment, these sites have to be located very close to the surface. The inconsistency of our slab calculation as shown in Fig. 5(d)-5(f) with the experiment argues against possible intercalation into the gap between the topmost Sn and Sb layers that has the smallest inter-layer spacing in Sn_4Sb_3 (Fig. 1(b)). On the other hand, the intercalants are more likely located within the gap between the topmost two Sn–Sb bilayers, which has the largest interlayer spacing within the septuple-layer block. Because Sn and Sb have very similar atomic numbers (50 vs. 51) and electronegativity (1.96 vs. 2.05), the latter gap has a mixed covalent and vdW character, thereby facilitating possible intercalation therein. Intercalation at interstitial sites in a covalent bonding environment was previously proposed to occur in Bi_2Se_3, based on some subtle spectral signatures observed [33,34]. The case presented here in Sn_4Sb_3 is much clearer, with distinct spectral features identifiable for both the surface adsorption and interstitial intercalation as a function of Cs dosing (Fig. 4(b)). Nevertheless, questions remain open as to why the intercalation-related Cs core level feature is resided at a lower binding energy and has a larger linewidth than the one related to the adsorption. Further examinations of the emission angle dependence of the Cs as well as other core levels at different Cs dosages are needed for scrutinizing the proposed possibility for intercalation in the system. While intercalations can occur at different sites in different chemical environments that can lead to core level replica at different energies, it is likely that the other dosing channel that dominates at low to medium dosages in the observed dosing evolution of the Cs core levels (Fig. 4(c)) is the surface adsorption, which has generally been found in most dosing studies especially in the low dosage regime [2,15,35,36].

A salient observation in the dosing evolution is the suppression of the surface band splitting between SS1′ and SS1″ with increasing dosage. This observation can be captured, as we described earlier, by both scenarios, i.e., the interstitial intercalation, which corresponds to the case with Cs placed at the bottom of the Sn–Sb bilayer (Fig. 5(c)), and the surface adsorption, which corresponds to the case with Cs placed on top of the bilayer (Fig. 5(b)). Given the finite peak widths experimentally observed, it is difficult to determine the quantitative amount of remnant splitting at high Cs dosages. It is therefore not possible to distinguish between the two scenarios based on this observation alone. Nevertheless, the remarkable difference between the two cases as revealed by the simplified calculations suggests that the Sn–Sb intra-bilayer hybridization, whose strength can be reflected by the SS1′-SS1″ band splitting [26], is sensitive to the band bending potential gradient at the surface and its directions. Our finding may provide a clue to decipher the mechanism for the changing SS1′-SS1″ band splitting with Cs dosing and understand why band splitting is notably absent on other surface-state bands.

Taken together, our experiment along with calculations support the occurrence of Cs intercalation at interstitial sites within the structural block with covalent bonding in Sn_4Sb_3, in addition to the conventional Cs surface adsorption. This intercalation likely results in a partial electronic decoupling between the topmost Sn and Sb layers on top of their structural decoupling from the bulk (with Cs atoms sitting between the Sn–Sb bilayer and the rest of the bulk). Such an unexpected effective dimensionality reduction might hold the key to understanding the effect of quantum confinement on the surface electronic structure in this system and promise its novel surface properties different from the bulk.

5. Conclusion

We have presented an ARPES study of the effect of *in-situ* Cs dosing on the surface electronic structure of Sn_4Sb_3. As the chemical potential of the system increases upon Cs dosing, we observed an electronic structure evolution that goes beyond a simple rigid band shift model. Different surface bands exhibit energy shifts in comparable amounts while bulk bands undergo variable but overall less pronounced shifts in energy, with some presenting increasingly sharp spectral line shapes. These observations are manifestations of quantum confinement of electronic states near the surface due to Cs decoration. Evolution of Cs 5*p* core level as functions of Cs dosage and photoelectron emission angle reveals two distinct channels for Cs dosing, with the deposition on the sample surface that dominates at low dosages and the intercalation underneath the sample surface that dominates at high dosages. Concomitant with Cs dosing, we observe a gradual suppression of a surface band splitting, which we show can be reasonably captured by simplified first-principles calculations for the deposition/intercalation on either side of the first Sn–Sb bilayer. Such intercalation likely causes a partial electronic decoupling between the topmost Sn and Sb layers on top of their structural decoupling from the bulk. Our finding highlights the possibility of a unique dimensionality reduction in Sn_4Sb_3 caused by Cs intercalation at interstitial sites that promises its novel surface properties different from the bulk.

Declaration of competing interest

The authors declare that they have no known competing financial interests or personal relationships that could have appeared to influence the work reported in this paper.

Acknowledgments

This work was supported by the National Natural Science Foundation of China (Grant No. 11874053), Zhejiang Provincial Natural Science Foundation of China (LZ19A040001) and the Instrumentation and Service Center for Physical Sciences (ISCPS) at Westlake University.

References

[1] W. Wen, G. Zhao, C. Hong, Z. Song, R.-H. He, 3D negative electronic compressibility as a new emergent phenomenon, J. Supercond. Nov. Magnetism 33 (2020) 229–239, https://doi.org/10.1007/s10948-019-05325-z.

[2] Z.K. Liu, B. Zhou, Y. Zhang, Z.J. Wang, H.M. Weng, D. Prabhakaran, S.K. Mo, Z. X. Shen, Z. Fang, X. Dai, Z. Hussain, Y.L. Chen, Discovery of a three-dimensional topological Dirac semimetal, Na3Bi, Science 343 (2014) 864–867, https://doi.org/10.1126/science.1245085.

[3] D.F. Liu, A.J. Liang, E.K. Liu, Q.N. Xu, Y.W. Li, C. Chen, D. Pei, W.J. Shi, S.K. Mo, P. Dudin, T. Kim, C. Cacho, G. Li, Y. Sun, L.X. Yang, Z.K. Liu, S.S.P. Parkin, C. Felser, Y.L. Chen, Magnetic Weyl semimetal phase in a Kagomé crystal, Science 365 (2019) 1282–1285, https://doi.org/10.1126/science.aav2873.

[4] M. Hossain, J. Mottershead, D. Fournier, A. Bostwick, J. McChesney, E. Rotenberg, R. Liang, W. Hardy, G. Sawatzky, I. Elfimov, D. Bonn, A. Damascelli, In situ doping control of the surface of higherature superconductors, Nat. Phys. 4 (2008) 527–531, https://doi.org/10.1038/nphys998.

[5] Y.K. Kim, O. Krupin, J.D. Denlinger, A. Bostwick, E. Rotenberg, Q. Zhao, J. F. Mitchell, J.W. Allen, B.J. Kim, Fermi arcs in a doped pseudospin-1/2 Heisenberg antiferromagnet, Science 345 (2014) 187–190, https://doi.org/10.1126/science.1251151.

[6] M. Kang, B. Kim, S.H. Ryu, S.W. Jung, J. Kim, L. Moreschini, C. Jozwiak, E. Rotenberg, A. Bostwick, K.S. Kim, Universal mechanism of band-gap engineering in transition-metal dichalcogenides, Nano Lett. 17 (2017) 1610–1615, https://doi.org/10.1021/acs.nanolett.6b04775.

[7] J.M. Riley, W. Meevasana, L. Bawden, M. Asakawa, T. Takayama, T. Eknapakul, T. K. Kim, M. Hoesch, S.K. Mo, H. Takagi, T. Sasagawa, M.S. Bahramy, P.D.C. King, Negative electronic compressibility and tunable spin splitting in WSe2, Nat. Nanotechnol. 10 (2015) 1043–1047, https://doi.org/10.1038/nnano.2015.217.

[8] H.M. Benia, C. Lin, K. Kern, C.R. Ast, Reactive chemical doping of the Bi2Se3 topological insulator, Phys. Rev. Lett. 107 (2011) 177602, https://doi.org/10.1103/PhysRevLett.107.177602.

[9] M.S. Bahramy, P.D.C. King, A. de la Torre, J. Chang, M. Shi, L. Patthey, G. Balakrishnan, P. Hofmann, R. Arita, N. Nagaosa, F. Baumberger, Emergent quantum confinement at topological insulator surfaces, Nat. Commun. 3 (2012) 1159, https://doi.org/10.1038/ncomms2162.

[10] J. Kim, S.S. Baik, S.H. Ryu, Y. Sohn, S. Park, B.-G. Park, J. Denlinger, Y. Yi, H. J. Choi, K.S. Kim, Observation of tunable band gap and anisotropic Dirac semimetal state in black phosphorus, Science 349 (2015) 723–726, https://doi.org/10.1002/chin.201546005.

[11] S.S. Baik, K.S. Kim, Y. Yi, H.J. Choi, Emergence of two-dimensional massless Dirac fermions, chiral pseudospins, and Berry's phase in potassium doped few-layer black phosphorus, Nano Lett. 15 (2015) 7788–7793, https://doi.org/10.1021/acs.nanolett.5b04106.

[12] J. Kim, S.S. Baik, S.W. Jung, Y. Sohn, S.H. Ryu, H.J. Choi, B.J. Yang, K.S. Kim, Two-Dimensional Dirac fermions protected by space-time inversion symmetry in black phosphorus, Phys. Rev. Lett. 119 (2017) 226801, https://doi.org/10.1103/PhysRevLett.119.226801.

[13] S.W. Jung, S.H. Ryu, W.J. Shin, Y. Sohn, M. Huh, R.J. Koch, C. Jozwiak, E. Rotenberg, A. Bostwick, K.S. Kim, Black phosphorus as a bipolar pseudospin semiconductor, Nat. Mater. 19 (2020) 277–281, https://doi.org/10.1038/s41563-019-0590-2.

[14] T. Eknapakul, P.D.C. King, M. Asakawa, P. Buaphet, R.H. He, S.K. Mo, H. Takagi, K. M. Shen, F. Baumberger, T. Sasagawa, S. Jungthawan, W. Meevasana, Electronic structure of a quasi-freestanding MoS2 monolayer, Nano Lett. 14 (2014) 1312–1316, https://doi.org/10.1021/nl4042824.

[15] O.J. Clark, F. Mazzola, J. Feng, V. Sunko, I. Marković, L. Bawden, T.K. Kim, P.D. C. King, M.S. Bahramy, Dual quantum confinement and anisotropic spin splitting in the multivalley semimetal PtSe2, Phys. Rev. B 99 (2019), 045438, https://doi.org/10.1103/PhysRevB.99.045438.

[16] Y. Nakata, K. Sugawara, A. Chainani, K. Yamauchi, K. Nakayama, S. Souma, P. Y. Chuang, C.M. Cheng, T. Oguchi, K. Ueno, T. Takahashi, T. Sato, Dimensionality reduction and band quantization induced by potassium intercalation in 1T−HfTe2, Phys. Rev. Mater. 3 (2019), 071001, https://doi.org/10.1103/PhysRevMaterials.3.071001.

[17] S. Cho, B.S. Kim, B. Kim, W. Kyung, J. Seo, M. Park, J.W. Jeon, K. Tanaka, J. D. Denlinger, C. Kim, D. Odkhuu, B.H. Kim, S.R. Park, Electronic-dimensionality reduction of bulk MoS2 by hydrogen treatment, Phys. Chem. Chem. Phys. 20 (2018) 23007–23012, https://doi.org/10.1039/c8cp02365d.

[18] H.F. Yang, L.X. Yang, Z.K. Liu, Y. Sun, C. Chen, H. Peng, M. Schmidt, D. Prabhakaran, B.A. Bernevig, C. Felser, B.H. Yan, Y.L. Chen, Topological lifshitz transitions and Fermi arc manipulation in Weyl semimetal NbAs, Nat. Commun. 10 (2019) 3478, https://doi.org/10.1038/s41467-019-11491-4.

[19] K. Rossnagel, Suppression and emergence of charge-density waves at the surfaces of layered 1T-TiSe2 and 1T-TaS2 by in situ Rb deposition, New J. Phys. 12 (2010) 125018, https://doi.org/10.1088/1367-2630/12/12/125018.

[20] T. Eknapakul, I. Fongkaew, S. Siriroj, W. Jindata, S. Chaiyachad, S.K. Mo, S. Thakur, L. Petaccia, H. Takagi, S. Limpijumnong, W. Meevasana, Direct observation of strain-induced orbital valence band splitting in HfSe2 by sodium intercalation, Phys. Rev. B 97 (2018) 201104, https://doi.org/10.1103/PhysRevB.97.201104.

[21] B. Liu, X. Zhu, G. Xiao, Y. Liu, J. Wu, Y. Cui, Q. Zhu, S. Wu, X. Lu, G.-h. Cao, Z. Ren, Flux growth, mixed valence state and superconductivity of Sn4Sb3 intermetallic crystals, Intermetallics 137 (2021) 107301, https://doi.org/10.1016/j.intermet.2021.107301.

[22] B. Liu, C. Xiao, Q. Zhu, J. Wu, Y. Cui, H. Wang, Z. Wang, Y. Lu, Z. Ren, G.-h. Cao, Superconducting phase diagram and nontrivial band topology of structurally modulated Sn1−xSbx, Phys. Rev. Mater. 3 (2019), 084603, https://doi.org/10.1103/PhysRevMaterials.3.084603.

[23] P.E. Blöchl, Projector augmented-wave method, Phys. Rev. B 50 (1994) 17953–17979, https://doi.org/10.1103/PhysRevB.50.17953.

[24] G. Kresse, J. Furthmüller, Efficient iterative schemes for ab initio total-energy calculations using a plane-wave basis set, Phys. Rev. B 54 (1996) 11169–11174, https://doi.org/10.1103/PhysRevB.54.11169.

[25] J.P. Perdew, K. Burke, M. Ernzerhof, Generalized gradient approximation made simple, Phys. Rev. Lett. 77 (1996) 3865–3868, https://doi.org/10.1103/PhysRevLett.77.3865.

[26] W. Wen, C. Hua, B. Liu, C. Hong, G. Zhao, Z. Song, Y. Lu, Z. Ren, R.-H. He, Angle-resolved photoemission spectroscopy study of the electronic structure evolution in Sn4X3 (X = P, As, Sb), Appl. Surf. Sci. 569 (2021) 150980, https://doi.org/10.1016/j.apsusc.2021.150980.

[27] N. Nagamura, K. Horiba, S. Toyoda, S. Kurosumi, T. Shinohara, M. Oshima, H. Fukidome, M. Suemitsu, K. Nagashio, A. Toriumi, Direct observation of charge transfer region at interfaces in graphene devices, Appl. Phys. Lett. 102 (2013) 241604, https://doi.org/10.1063/1.4808083.

[28] A. Jablonski, C.J. Powell, Effective attenuation lengths for different quantitative applications of X-ray photoelectron spectroscopy, J. Phys. Chem. Ref. Data 49 (2020), 033102, https://doi.org/10.1063/5.0008576.

[29] A.V. Fedorov, N.I. Verbitskiy, D. Haberer, C. Struzzi, L. Petaccia, D. Usachov, O. Y. Vilkov, D.V. Vyalikh, J. Fink, M. Knupfer, B. Buchner, A. Gruneis, Observation of a universal donor-dependent vibrational mode in graphene, Nat. Commun. 5 (2014) 3257, https://doi.org/10.1038/ncomms4257.

[30] J. Cai, W. Jolie, C.C. Silva, M. Petrović, C. Schlueter, T. Michely, M. Kralj, T.-L. Lee, C. Busse, Modifying the geometric and electronic structure of hexagonal boron nitride on Ir(111) by Cs adsorption and intercalation, Phys. Rev. B 98 (2018) 195443, https://doi.org/10.1103/PhysRevB.98.195443.

[31] X. Duan, Z. Liu, B.M. Hanrahan, W. Zhu, S. Liu, Designing xenes with two-dimensional triangular lattice, Phys. Rev. Mater. 4 (2020) 124003, https://doi.org/10.1103/PhysRevMaterials.4.124003.

[32] Z. El Youbi, S.W. Jung, S. Mukherjee, M. Fanciulli, J. Schusser, O. Heckmann, C. Richter, J. Minár, K. Hricovini, M.D. Watson, C. Cacho, Bulk and surface electronic states in the dosed semimetallic HfTe2, Phys. Rev. B 101 (2020) 235431, https://doi.org/10.1103/PhysRevB.101.235431.

[33] Y.-L. Wang, Y. Xu, Y.-P. Jiang, J.-W. Liu, C.-Z. Chang, M. Chen, Z. Li, C.-L. Song, L.-L. Wang, K. He, X. Chen, W.-H. Duan, Q.-K. Xue, X.-C. Ma, Structural defects and electronic properties of the Cu-doped topological insulator Bi2Se3, Phys. Rev. B 84 (2011), 075335, https://doi.org/10.1103/PhysRevB.84.075335.

[34] H.-J. Noh, J. Jeong, E.-J. Cho, J. Park, J.S. Kim, I. Kim, B.-G. Park, H.-D. Kim, Controlling the evolution of two-dimensional electron gas states at a metal/Bi2Se3 interface, Phys. Rev. B 91 (2015) 121110, https://doi.org/10.1103/PhysRevB.91.121110.

[35] M. Petrović, I. Šrut Rakić, S. Runte, C. Busse, J.T. Sadowski, P. Lazić, I. Pletikosić, Z.-H. Pan, M. Milun, P. Pervan, N. Atodiresei, R. Brako, D. Šokčević, T. Valla, T. Michely, M. Kralj, The mechanism of caesium intercalation of graphene, Nat. Commun. 4 (2013) 2772, https://doi.org/10.1038/ncomms3772.

[36] G. Wang, X. Zhu, J. Wen, X. Chen, K. He, L. Wang, X. Ma, Y. Liu, X. Dai, Z. Fang, J. Jia, Q. Xue, Atomically smooth ultrathin films of topological insulator Sb2Te3, Nano Res. 3 (2010) 874–880, https://doi.org/10.1007/s12274-010-0060-2.